

# Electronic Instability and Anharmonicity in SnSe

Jiawang Hong<sup>1,\*</sup> and Olivier Delaire<sup>1,2,†</sup>

<sup>1</sup>*Materials Science and Technology Division, Oak Ridge National Laboratory, Oak Ridge, TN 37831*

<sup>2</sup>*Mechanical Engineering and Materials Science Department, Duke University, Durham, NC 27708*

The binary compound SnSe exhibits record high thermoelectric performance, largely because of its very low thermal conductivity. The origin of the strong phonon anharmonicity leading to the low thermal conductivity of SnSe is investigated through first-principles calculations of the electronic structure and phonons. It is shown that a Jahn-Teller instability of the electronic structure is responsible for the high-temperature lattice distortion between the Cmcm and Pnma phases. The coupling of phonon modes and the phase transition mechanism are elucidated, emphasizing the connection with hybrid improper ferroelectrics. This coupled instability of electronic orbitals and lattice dynamics is the origin of the strong anharmonicity causing the ultralow thermal conductivity in SnSe. Exploiting such bonding instabilities to generate strong anharmonicity may provide a new rational to design efficient thermoelectric materials.

PACS numbers: 63.20.Ry, 71.20.-b

Quasiparticle couplings such as phonon-phonon and electron-phonon interactions play a central role in condensed matter physics. In energy materials, it is critical to understand the interaction between phonons and the electronic structure, and how the chemical bonding impacts atomic vibrations, in order to control both thermodynamics and transport properties. The origin of the strongly anharmonic bonding in binary metal chalcogenides is the subject of renewed interest, both fundamentally and in connection with ferroelectric and thermoelectric properties. SnSe in particular is currently attracting strong interest, owing to the recent discovery of its record-high thermoelectric efficiency. [1, 2] This high thermoelectric conversion efficiency results in part from an ultra-low thermal conductivity. [1, 3–5]

Our recent inelastic neutron scattering (INS) measurements have shown that the ultralow thermal conductivity of SnSe arises from strongly anharmonic phonons near a lattice instability. [6] A continuous structural phase transition occurs at  $T_c \sim 805$  K, associated to the condensation of a soft phonon mode, which remains strongly anharmonic over a broad temperature range below the transition. The soft mode is the lowest-energy transverse optical (TO) phonon mode at the zone center in the low-symmetry phase ( $T < T_c$ ), but stems from a zone-boundary mode in the high-symmetry phase, leading to a doubling of the unit cell on cooling through  $T_c$ . [6, 7] The low-symmetry phase is non-polar.

Thus, the behavior of SnSe is reminiscent of, while significantly different from, the ferroelectric instability in the binary rocksalt chalcogenides (PbTe, SnTe, GeTe). Upon cooling, SnTe and GeTe undergo a displacive distortion from the cubic phase to a ferroelectric rhombohedral structure, corresponding to the condensation of the degenerate transverse-optic branch at the zone center ( $\Gamma$ ). [8] In the incipient ferroelectric PbTe, the TO mode softening is only partial and the rocksalt phase remains stable. As previously investigated, the soft-mode

suppresses the thermal conductivity of rocksalt chalcogenides by scattering the acoustic phonons through anharmonic phonon-phonon interactions, which is beneficial to improve the thermoelectric performance. [9–15]

Resonant bonding and lone-pair electrons have both been associated with the lattice instability in the rocksalt compounds, as well as in related phase-change materials. [15–17] The compound SnSe is structurally quite distinct from the rocksalts, however, with a layered structure giving rise to strongly anisotropic electronic structure, lattice dynamics, and electrical and thermal transport properties. It can be viewed as intermediate between the rocksalt structure and the quasi-two-dimensional transition metal dichalcogenides, such as MoS<sub>2</sub> and NbSe<sub>2</sub>.

SnSe crystallizes in a layered orthorhombic structure (Pnma) at ambient temperature, with two bilayers along the  $a$  direction. Upon heating, it transforms continuously to the higher symmetry Cmcm phase at  $T_c \sim 800$  K, [7, 18] as illustrated in Fig. 1. This second-order phase transition corresponds to the condensation of the TO soft phonon mode of  $A_g$  symmetry at the Brillouin zone center ( $\Gamma$ ) in the Pnma phase (see Fig. 2f), as predicted based on symmetry arguments, [7] and experimentally observed with INS. [6] However, a direct connection between electronic structure and the strong anharmonicity in SnSe, which underpins its ultra-low thermal conductivity, has remained elusive. This question is deeply connected with the phonon mode instability and the microscopic mechanism of the phase transition. In this Letter, we show how the lattice instability in SnSe arises from a Jahn-Teller-like electronic instability in the Cmcm phase, which results in very large anharmonicity and ultra-low thermal conductivity. In addition, we investigate the anharmonically coupled zone-boundary and zone-center phonon modes, which drive the phase transition from Cmcm to Pnma on cooling across  $T_c$ .

The Pnma and Cmcm structures can be viewed as variants of the rocksalt structure. In both phases, the Sn-Se

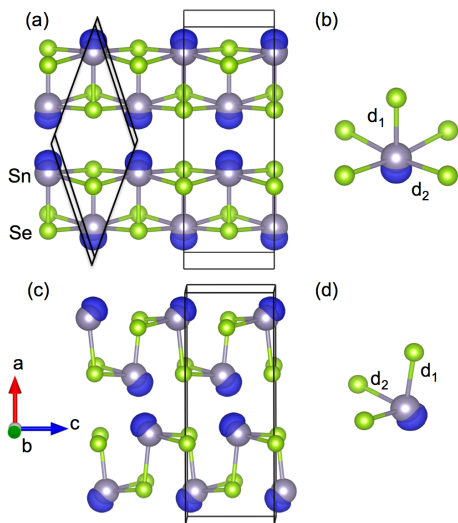


FIG. 1: (Color online) Crystal structure of SnSe in Cmcm (a) and Pnma (c) phases, illustrating the double bilayer structure and Pnma distortion, and corresponding Sn-Se bonding state (b,d). Sn atoms are in grey and Se atoms in green.  $d_1$  and  $d_2$  are labels for bonds out-of-plane and in-plane, respectively. The crystal axes in the Cmcm structure are chosen to match the Pnma phase, in order to facilitate the comparison. The conventional unit cell is indicated by the black box, while the diamond shape indicates the primitive cell for Cmcm. The blue caps on Sn atoms represent the isosurface of electron localization function (ELF=0.93), showing the lone pair electrons of Sn atoms.

bilayer is a rocksalt fragment, with the two bilayers offset along the  $\langle 110 \rangle_{\text{cubic}}$  direction, compared to rocksalt. The Pnma phase is further distorted by an off-centering of Sn atoms in their coordination polyhedra. Related distorted structures also appear in the MX family (M=Ge, Sn; X=S, Se, Te), while PbX always crystallizes as rock salt at ambient pressure. [19] In early investigations, Tremel and Hoffmann [20] rationalized the chemical bonding in SnS based on tight-binding electronic structure calculations and showed that, within their 2-dimensional approximation, the mixing of the conduction and valence bands play an important role in SnS. Waghmare *et al.* focused on the stereochemical activity of cation lone pair electrons in connection with the structural distortion in several MX compounds. [16] Here, we reveal the origin of strong anharmonicity in SnSe as a coupling of specific phonons with the bonding instability, using accurate first-principles simulations.

Computations were performed in the framework of density functional theory (DFT) as implemented in the Vienna Ab initio simulation package (VASP) [21, 22]. All calculations used a plane-wave cutoff of 500 eV. We used the local-density approximation (LDA) and projector-augmented-wave (PAW) potentials, explicitly including 4 valence electrons for Sn ( $5s^2 5p^2$ ) and 6 for Se ( $4s^2$

$4p^4$ ). Our calculations used LDA rather than the generalized gradient approximation (GGA) used in Refs. 4, 23, since we previously observed that LDA phonon dispersions match better with INS measurements.[6] We used experimental structures [7] as starting configurations and relaxed the lattice parameters and atomic positions until all atomic force components were smaller than  $1 \text{ meV/\AA}$ . The phonon dispersions were calculated with VASP and Phonopy [24], using  $3 \times 5 \times 5$  supercells (larger in-plan size is tested, see Fig.S1). Based on convergence studies, we used  $6 \times 12 \times 12$  and  $2 \times 4 \times 4$  Monkhorst-Pack electronic  $k$ -point meshes for the unit cell and supercell, respectively. We used the software Lobster to compute the crystal orbital hamiltonian populations (COHP). [25–27]

*Lattice instability.*— The phonon dispersions (see Fig. 2a) in Cmcm, in the harmonic approximation, show soft modes at  $\Gamma$  ( $B_{1u}$  mode) and the zone boundary  $Y$  point (referred to as  $Y$  mode thereafter [28]). Similar phonon dispersion is reported in Ref. 23. At  $\Gamma$ , the soft  $B_{1u}$  mode is “ferroelectric-like”: all Sn atoms move toward  $+b$ , while all Se atoms move toward  $-b$ . In the  $Y$  mode, Sn atoms in one bilayer move along  $+c$  and Sn atoms in the other bilayer move along  $-c$  ( $b$  and  $c$  are in Pnma coordinates here, see Fig. 2d). We describe in details below how this zone-boundary  $Y$  mode overlaps with the structural distortion to Pnma, and couples to a Jahn-Teller-like electronic instability. The  $Y$  point in Cmcm becomes  $\Gamma$  in Pnma and this soft mode reappears as the  $A_g$  transverse optical mode in Pnma (Ref. [6]).

The calculated frozen-phonon potentials for the soft  $B_{1u}$  and  $Y$  modes are shown in Fig. 2b. Both modes exhibit a characteristic “double-well” profile (the potentials are symmetric and only the positive side is shown). However, we note that the  $B_{1u}$  mode only has a very shallow well ( $\Delta E = 0.3 \text{ meV/atom}$ ), while the  $Y$  mode shows a deeper double-well ( $\Delta E = 1.25 \text{ meV/atom}$ ), although still small. The potential energy surface  $f(Q_Y, Q_{B_{1u}})$  computed from DFT is shown in supplementary Fig.S2. It reveals that these two modes compete with each other, since the energy has minima on the  $Y$  or  $B_{1u}$  axes, but increases for combinations. The  $Y$  mode exhibits a stronger instability and it is the primary order parameter for the distortion along  $c$  that produces the Pnma structure, as experimentally observed. Therefore, in the following we will mostly focus on  $Y$  mode and its coupling with  $A_g$  mode.

According to the phase relationship between the experimental Pnma and Cmcm structures, the zone-boundary soft mode at  $Y$  is not sufficient to generate the distortion observed, as some motion of atoms along  $a$  is also needed (normal to layers). This additional component is provided by an  $A_g$  mode at  $\Gamma$  with energy  $8.9 \text{ meV}$  (see Fig. 2e). We investigate the coupling of  $A_g$  and  $Y$  modes, by expanding the potential energy in phonon normal co-

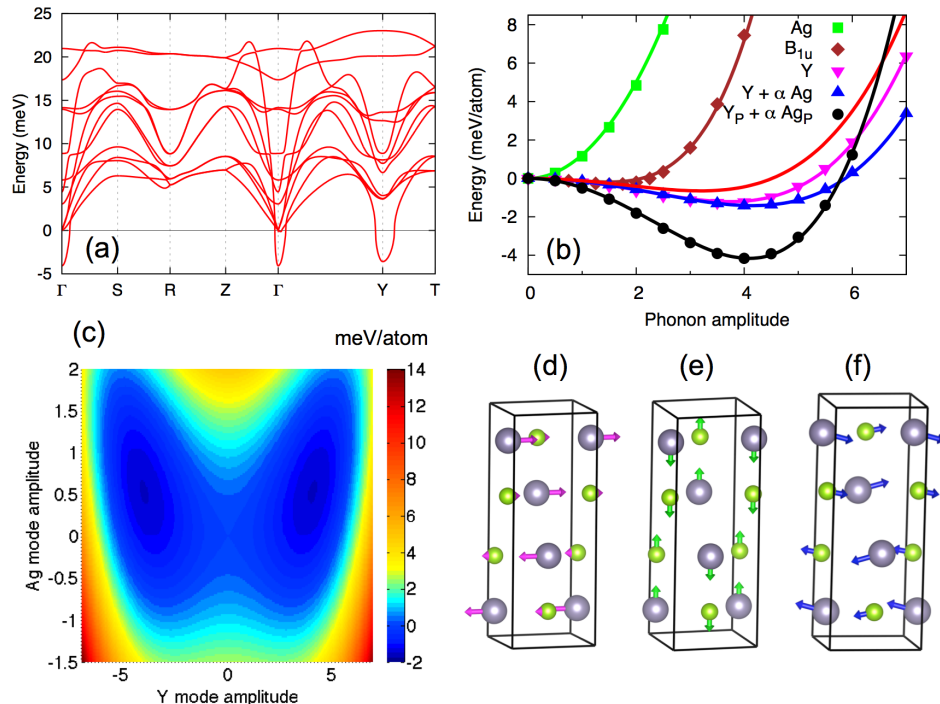


FIG. 2: (Color online) Phonon dispersions in Cmcm phase (a) and frozen-phonon potentials (b) for the soft modes at zone boundary ( $Y$  mode) and the zone center ( $B_{1u}$  mode and  $A_g$  mode), and the combined modes of  $Y + \alpha A_g$  in Cmcm phase and pseudo Pnma phase ( $Y_P + \alpha A_{gP}$ ), in which the energy without distortion was shifted to the same energy as undistorted Cmcm phase (set as 0) for clear comparison. The symbols are *ab initio* energies and the curves are fitted from Landau theory according to Eq.(1-3). The red curve is a fit without the anharmonic coupling between  $A_g$  and  $Y$ . (c) is the frozen phonon energy for different coupling between  $Y$  and  $A_g$  mode. The unit for the right color scale is meV/atom. (d),(e) illustrate the phonon eigenvectors for  $Y$ ,  $A_g$  modes in Cmcm phase, (f) is for the  $A_g$  soft mode in Pnma phase. See text for more details.

ordinates  $Q_n$  for phonon mode  $n$  ( $n = Y, B_{1u}, A_g$ ):

$$f_n(Q_n) = a_n Q_n^2 + b_n Q_n^3 + c_n Q_n^4 \quad (1)$$

$$f_{\text{woc}}(Q_Y, Q_{A_g}) = f_Y(Q_Y) + f_{A_g}(Q_{A_g}) \quad (2)$$

$$f_{\text{wc}}(Q_Y, Q_{A_g}) = f_Y(Q_Y) + f_{A_g}(Q_{A_g}) + dQ_{A_g}Q_Y^2 + eQ_Y^2Q_{A_g}. \quad (3)$$

Here we have made the approximation of truncating the expansion systematically at overall fourth order, and  $Q_n = (Q_n/\sqrt{Nm_j})\text{Re}[\mathbf{e}_j \exp(i\mathbf{q} \cdot \mathbf{r}_{jl})]$ ,  $N$  is the number of atoms in the supercell,  $m_j$  is the mass of atom  $j$ ,  $\mathbf{q}$  is the wavevector,  $\mathbf{r}_{jl}$  is the position of atom  $j$  in unit cell  $l$ , and  $\mathbf{e}_j$  is the  $j$ -th atom component of the eigenvector.  $Q_n$  is the phonon amplitude of mode  $n$ , and  $a_n, b_n, c_n, d, e$  are numerical parameters used to fit DFT energies, with  $b_n = 0$  for  $Y$  and  $B_{1u}$  modes, owing to mirror symmetry along  $c$  and  $b$  directions in Cmcm, respectively. Here,  $f_Y(Q_Y)$  and  $f_{A_g}(Q_{A_g})$  are the frozen phonon potentials along individual coordinates, while  $f(Q_Y, Q_{A_g})$  corresponds to the superposition of these two modes. We attempt to express the latter both without coupling,  $f_{\text{woc}}(Q_Y, Q_{A_g})$  (Eq.(2)), and with mode coupling through  $d$  and  $e$  terms in Eq.(3), [29] denoted  $f_{\text{wc}}(Q_Y, Q_{A_g})$ . Such couplings of zone-center and zone-boundary modes are of

strong current interest in improper hybrid ferroelectric oxides. [30, 31]

The potential energy surface  $f(Q_Y, Q_{A_g})$  computed from DFT is shown in Fig. 2c. As can be seen from this figure, the two modes are clearly coupled, with a diagonal minimum for the energy at an amplitude ratio  $\alpha = Q_{A_g}/Q_Y = 0.15$ , close to the experimental value of the structural distortion  $\alpha \simeq 0.2$ . The DFT energies (markers) in Fig. 2b are fit well using Eq.(1-3), shown as lines on the same figure, indicating the model is appropriate. We note for  $d = e = 0$  (i.e. without coupling between  $Q_Y$  and  $Q_{A_g}$ ), the resulting energy curve for  $Q_{A_g} = 0.2 \times Q_Y$  (red curve) is clearly higher than for pure  $Y$  mode. A satisfactory fit requires the anharmonic coupling terms in Eq.(3), as shown by the blue curve. We also plot the frozen-phonon potential for the  $A_g$  mode alone and the linear combination with  $Q_{A_g} = 0.2 \times Q_Y$ . This shows that the potential for  $A_g$  alone is stable and increases sharply with phonon amplitude, while the combined mode reaches a lower energy than the pure  $Y$  mode. These results clearly establish the importance of anharmonic coupling between  $Y$  and  $A_g$  modes in SnSe.

We note that even the combined  $Y + A_g$  distortion lowers the energy by only 1.45 meV/atom, how-

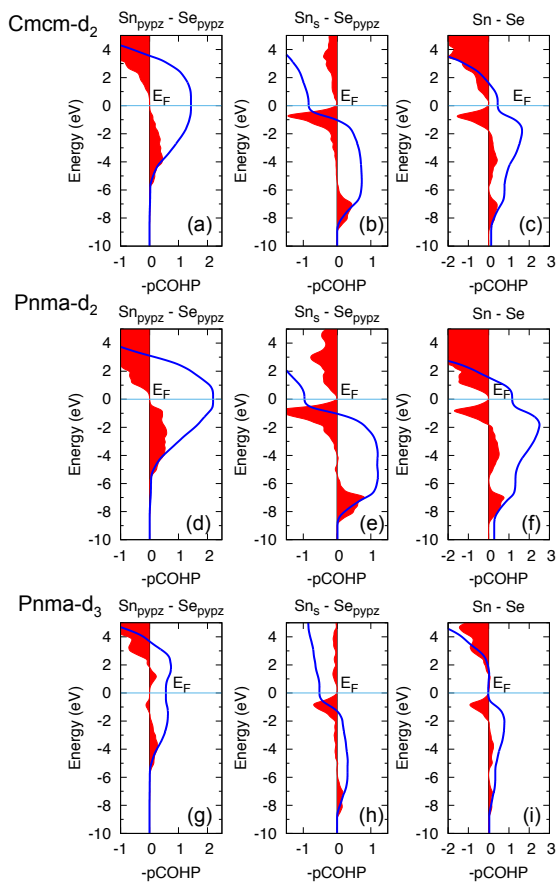


FIG. 3: (Color online) COHP calculation for Cmcm  $d_2$  bond (top panels) and Pnma  $d_2$  bond (middle panels) and Pnma  $d_3$  bond (bottom panels). The first column (a,d,g) is the bonding interaction between in-plane orbitals Sn-5p and Se-4p; the second column (b,e,h) is the bonding and anti-bonding interaction between lone pairs Sn-5s and in-plane Se- $p$  orbitals; the third column (c,f,i) is the total bonding interaction between Sn and Se atoms. Red filled curves are the  $-p\text{COHP}$  and the blue curves are  $-\text{IpCOHP}$ .

ever, much smaller than the total predicted energy difference between relaxed theoretical Cmcm and Pnma phases ( $\sim 5$  meV/atom), but this discrepancy can be attributed to the strain. We further explored the respective roles of atomic displacements and lattice strain by computing the distortion potential ( $Q_{\text{Ag}} + \alpha Q_{\text{Y}}$ ,  $\alpha = 0.2$ ) in a pseudo-phase based on the optimized Pnma lattice constants but with the Cmcm internal atomic positions. The result is shown in Fig. 2b (black markers and line). The depth of the double-well is now very close to the Cmcm-Pnma energy difference, confirming the importance of strain.

*Electronic instability.*— We now explain how the lattice instability and mode coupling result from the underlying electronic instability. We start by discussing the projected crystal orbital hamiltonian populations (pCOHP). The related approach of crystal orbital overlap population (COOP) analysis provides electron-resolved

TABLE I: Bond length ( $l$ ), IpCOHP ( $\xi$ ) and force constant ( $k$ ) for  $d_1$ ,  $d_2$  and  $d_3$  bonds in Cmcm and Pnma phases. Total IpCOHP for Sn polyhedron ( $d_1 + 2d_2 + 2d_3$ ) is also listed. The force constant is the average of in-plane component for  $d_2$  and  $d_3$  ( $k_{yy} + k_{zz}$ )/2 and axial component for  $d_1$  ( $k_{xx}$ ).  $l$  in  $\text{\AA}$ ,  $\xi$  in eV,  $k$  in  $\text{eV}/\text{\AA}^2$ .

		$d_1$	$d_2$	$d_3$	Total
Cmcm	$l$	2.71	2.96	2.96	—
	$\xi$	-0.96	-0.45	-0.45	-2.76
	$k$	-3.92	-0.35	-0.35	—
Pnma	$l$	2.74	2.79	3.20	—
	$\xi$	-0.75	-1.16	0.02	-3.03
	$k$	-3.31	-1.32	0.01	—

bonding information. But we chose the COHP to provide energy-resolved local bonding information, well suited to probe the electronic instability. [25–27] The pCOHP was calculated for bonds  $d_1$ ,  $d_2$  (see notation in Fig. 1), in both Cmcm and Pnma phases and  $d_3$  corresponding to the two elongated in-plane bonds in Pnma. The integrated pCOHP (IpCOHP) is also calculated to probe the energetics of bonding and antibonding interactions, as its magnitude correlates with the extent of covalency and relative bonding strength (the more negative value, the stronger covalent bonding strength). The total pCOHP and IpCOHP between the nearest Sn and Se and the main contribution from in-plane Sn  $p$  and Se  $p$  orbitals, and the Sn  $s$  and Se in-plane  $p$  orbitals are shown in Fig. 3. [32] The IpCOHP ( $\xi$ ), bond lengths ( $l$ ) and force constants ( $k$ ) for  $d_1$ ,  $d_2$  and  $d_3$  are compared for both phases in Table I. A schematic illustration and explanation of negative force-constants in this table can be found in Fig.S3.

From Fig. 3, one can see that the most energetically favorable interactions are in-plane ( $yz$  plane) Sn 5p and Se 4p. The hybridization between Sn- $s$  and in-plane Se- $p$  shows strong occupied anti-bonding states just below the Fermi level. In Cmcm, four degenerate Sn-Se bonds share four electrons, forming identical “resonant” half-filled bonds along  $\langle 011 \rangle$ . This high-symmetry resonant bonding state is energetically unfavorable. In distorted Pnma at low  $T$ , a geometric distortion breaks the symmetry and causes two shorter ( $d_2$ ) and two longer ( $d_3$ ) bonds. The shorter  $d_2$  bonds enhance significantly the in-plane Sn- $p$  – Se- $p$  interactions (from  $\xi = -1.43$  to  $\xi = -2.20$  eV, Fig. 3a,d), as well as anti-bonding hybridization of Sn- $s$  and in-plane Se- $p$  to a lesser degree (from  $\xi = 0.84$  to  $\xi = 0.96$  eV, Fig. 3b,e). The  $d_2$  bond thus becomes much stiffer and the force-constant ( $k_{yy}^{d_2} + k_{zz}^{d_2}$ )/2 increases nearly four-fold from  $-0.35$   $\text{eV}/\text{\AA}^2$  to  $-1.32$   $\text{eV}/\text{\AA}^2$ , as shown in Table I. The IpCOHP for  $d_2$  bond decreases from  $-0.45$  eV in Cmcm is to  $-1.16$  eV in Pnma, showing significant strengthening of  $d_2$  bonds. Simultaneously, the  $d_3$  bonds weaken to near-zero IpCOHP and force-constant, indicating  $d_3$  breaks in the

Pnma phase, as the Sn coordination changes to a triangular pyramid with almost equal  $d_1$  and  $d_2$  bond lengths (see Fig. 1d and Fig.S5). This large difference between  $d_2$  and  $d_3$  causes the large non-linear forces (anharmonicity) for Sn motion along  $c$ , as the strongly anharmonic frozen phonon potential for  $Y$  and  $Y + \alpha A_g$  modes shows in Fig. 2b.

In contrast, the  $d_1$  bonding changes little between the two phases (Fig.S4). On cooling,  $d_1$  slightly elongates and its force-constant weakens a little, compatible with the IpCOHP. Again, the Sn  $5s$  and Se  $4p_x$  have occupied anti-bonding states just below the Fermi level ( $\xi = 0.49$  eV). However, the Sn  $5p_x$  and Se  $4p_x$  states are strongly bonding ( $\xi = -1.47$  eV) and overall the  $d_1$  bond is stable and does not change much through the transition. From Cmcm to Pnma, the total IpCOHP (summing over the Sn nearest-neighbor bonds) decreases from  $-2.76$  eV to  $-3.03$  eV (Table I), showing that the latter is electronically more stable. Therefore, the distortion is electronically driven by lowering the electronic energy through lifting the degeneracy of “resonant” bonding in the Cmcm phase, similar to a Jahn-Teller distortion. [33, 34]

Finally, we investigate the behavior of the Sn  $5s$  lone-pair electrons in the phase transition. In Fig. 1 and Fig.S5, the plots of electron localization functions (ELF) [35] clearly show that the Sn  $5s$  lone-pair electrons are stereochemically active in both phases. As discussed above, the Sn  $5s$  lone-pair combines with the Se  $4p$  states to form a bonding state at  $\sim -8$  eV and an occupied anti-bonding state at the top of the valence band. We also observe an admixture of states across the gap (see Fig.S6). The orbital-weighted band structure (Fig.S6) and projected density of states (Fig.S7) show that the bottom of the conduction band is mostly composed of Sn  $5p$  bands, while the top of the valence band is mainly derived from Sn  $5s$  and Se  $4p$  anti-bonding hybrids, as also evident in Fig. 3. Along the  $\Gamma$ -Y direction (Fig.S6), one can clearly see the mixture of conduction band and valence bands, which is also responsible for the stabilization of the lower symmetry Pnma, as previously suggested by Tremel and Hoffmann. [20].

This can be understood as Sn  $5p$  states and anti-bonding (Sn $5s$ -Se $4p$ )\* states mixing into a new bonding ( $m$ ) state and anti-bonding ( $m^*$ ) state, where  $m$  is just below  $E_F$  and the anti-bonding state above  $E_F$ . This stabilization is achieved by distorting from the rocksalt structure and mixing the valence and conduction bands [20]. The orbital stabilization requires asymmetric electron density where the lone pair distribution is projected away from the cation (Sn $^{2+}$ ) toward the interlayer void region. This is illustrated in Fig. 1d and Fig.S5.

In summary, the lattice distortion in SnSe is driven by a Jahn-Teller electronic instability, which results in strong anharmonicity of lattice dynamics. In particular, zone-boundary and zone-center phonon modes are an-

harmonically coupled, explaining the observed structural phase transition path from Cmcm to Pnma on cooling across  $T_c$ . This behavior is similar to coupled phonon instabilities in hybrid improper ferroelectrics, although the low- $T$  phase of SnSe remains non-polar. The instability of the in-plane resonant bonding in this quasi-two-dimensional structure is the chemical origin of the strong anharmonicity, and drives the Jahn-Teller distortion. This mechanism could provide a way to design materials with low thermal conductivity, suitable for the thermoelectric applications, by tuning the chemistry and orbital interactions.

This work was supported by the U.S. Department of Energy, Office of Science, Basic Energy Sciences, Materials Sciences and Engineering Division, through the Office of Science Early Career Research Program (PI Delaire). This research used resources of the Oak Ridge Leadership Computing Facility, which is supported by the Office of Science of the U.S. DOE.

---

\* Electronic address: hongj@ornl.gov

† Electronic address: olivier.delaire@duke.edu

- [1] L.-D. Zhao, S.-H. Lo, Y. Zhang, H. Sun, G. Tan, C. Uher, C. Wolverton, V. Dravid, and M. Kanatzidis, *Nature* **508**, 373 (2014).
- [2] L.-D. Zhao, G. Tan, S. Hao, J. He, Y. Pei, H. Chi, H. Wang, S. Gong, H. Xu, V. P. Dravid, et al., *Science* **351**, 141 (2016).
- [3] C.-L. Chen, H. Wang, Y.-Y. Chen, T. Day, and G. J. Snyder, *J. Mater. Chem. A* **2**, 11171 (2014).
- [4] J. Carrete, N. Mingo, and S. Curtarolo, *Appl. Phys. Lett.* **105**, 101907 (2014).
- [5] S. Sassi, C. Candolfi, J.-B. Vaney, V. Ohorodniichuk, P. Masschelein, A. Dauscher, and B. Lenoir, *Appl. Phys. Lett.* **104**, 212105 (2014).
- [6] C. W. Li, J. Hong, A. F. May, D. Bansal, S. Chi, T. Hong, G. Ehlers, and O. Delaire, *Nat. Phys.* **11**, 1063 (2015).
- [7] K. Adouby, C. Perez-Vicente, J. C. Jumas, R. Fourcade, and A. Abba Toure, *Z. Kristallogr.* **213**, 343 (1998).
- [8] W. Jantsch, in *Dynamical Properties of IV-VI Compounds* (Springer, 1983), vol. 99 of *Springer Tracts in Modern Physics*, pp. 1–50.
- [9] O. Delaire, J. Ma, K. Marty, A. F. May, M. A. McGuire, M.-H. Du, D. J. Singh, A. Podlesnyak, G. Ehlers, M. D. Lumsden, et al., *Nat. Mater.* **8**, 614 (2011).
- [10] Y. Zhang, X. Ke, P. R. C. Kent, J. Yang, and C. Chen, *Phys. Rev. Lett.* **107**, 175503 (2011).
- [11] T. Shiga, J. Shiomi, J. Ma, O. Delaire, T. Radzynski, A. Lusakowski, K. Esfarjani, and G. Chen, *Phys. Rev. B* **85**, 155203 (2012).
- [12] C. W. Li, J. Ma, H. B. Cao, A. F. May, D. L. Abernathy, G. Ehlers, C. Hoffmann, X. Wang, T. Hong, A. Huq, et al., *Phys. Rev. B* **90**, 214303 (2014).
- [13] C. W. Li, O. Hellman, J. Ma, A. F. May, H. B. Cao, X. Chen, A. D. Christianson, G. Ehlers, D. J. Singh, B. C. Sales, et al., *Phys. Rev. Lett.* **112**, 175501 (2014).
- [14] Y. Chen, X. Ai, and C. A. Marianetti, *Phys. Rev. Lett.* **113** (2014).

- [15] S. Lee, K. Esfarjani, T. Luo, J. Zhou, Z. Tian, and G. Chen, *Nat. Commun.* **5**, 3525 (2014).
- [16] U. V. Waghmare, N. A. Spaldin, H. C. Kandpal, and R. Seshadri, *Phys. Rev. B* **67**, 125111 (2003).
- [17] K. Shportko, S. Kremers, M. Woda, D. Lencer, J. Robertson, and M. Wuttig, *Nat. Mater.* **7**, 653 (2008).
- [18] T. Chattopadhyay, J. Pannetier, and H. Von-Schnering, *J. Phys. Chem. Solids* **47**, 879 (1986).
- [19] A. F. Wells, *Structural Inorganic Chemistry*, 4th ed. (Oxford University Press, Oxford, 1974).
- [20] W. Tremel and R. Hoffmann, *Inorg. Chem.* **26**, 118 (1987).
- [21] G. Kresse and J. Hafner, *Phys. Rev. B* **47**, 558 (1993).
- [22] G. Kresse and J. Furthmüller, *Comput. Mater. Sci.* **6**, 15 (1996).
- [23] J. M. Skelton, L. A. Burton, S. C. Parker, A. Walsh, C.-E. Kim, A. Soon, J. Buckeridge, A. A. Sokol, C. R. A. Catlow, A. Togo, et al., arXiv:1602.03762 [cond-mat] (2016).
- [24] A. Togo, F. Oba, and I. Tanaka, *Phys. Rev. B* **78**, 134106 (2008).
- [25] R. Dronskowski and P. E. Bloechl, *J. Phys. Chem.* **97**, 8617 (1993).
- [26] V. L. Deringer, A. L. Tchougreeff, and R. Dronskowski, *J. Phys. Chem. A* **115**, 5461 (2011), ISSN 1089-5639.
- [27] S. Maintz, V. L. Deringer, A. L. Tchougreeff, and R. Dronskowski, *J. Comput. Chem.* **34**, 2557 (2013).
- [28] In original Cmcm phase,  $Y$  point is (0.5,0.5,0), this  $Y$  point is (0.5,0,0.5) in our notation.
- [29] The coupling term  $Q_{A_g}^2 Q_Y$  is omitted because the energy is an even function for  $Y$  mode, due to mirror symmetry along  $c$  direction in the Cmcm phase.
- [30] E. Bousquet, M. Dawber, N. Stucki, C. Lichtensteiger, P. Hermet, S. Gariglio, J. M. Triscone, and P. Ghosez, *Nature* **452**, 732 (2008).
- [31] N. A. Benedek and C. J. Fennie, *Phys. Rev. Lett.* **106**, 107204 (2011).
- [32] We show the negative values ( $-\text{COHP}$  and  $-\text{IpCOHP}$ ) in the Fig.3 to resemble the normal COOP plots, i.e. drawing bonding contributions on the right of vertical line of  $\text{pCHOP}=0$ , and antibonding contribution on the left.
- [33] H. A. Jahn and E. Teller, *Proc. R. Soc. A* **161**, 220 (1937).
- [34] R. G. Pearson, *Proc. Natl. Acad. Sci. U.S.A.* **72**, 2104 (1975), ISSN 0027-8424, 1091-6490.
- [35] B. Silvi and A. Savin, *Nature* **371**, 683 (1994).

## Support Information: Electronic Instability and Anharmonicity in SnSe

The force constants  $k_{\alpha\beta}(jl, j'l')$  are defined in a conventional way: [1, 2]

$$k_{\alpha\beta}(jl, j'l') = \frac{\partial^2 V}{\partial r_\alpha(jl) \partial r_\beta(j'l')} = -\frac{\partial F_\beta(j'l')}{\partial r_\alpha(jl)} \quad (4)$$

where  $\alpha, \beta$  are the Cartesian indices,  $j, j'$  are the indices of atoms in a unit cell, and  $l, l'$  are the indices of unit cells,  $V$  is the potential energy as a function of atomic position  $\mathbf{r}(jl)$ . According to this definition, a negative force constant indicates that the force on atom ( $jl$ ) has the same direction as the displacement of atom ( $jl$ ). For example, if the displacement of atom ( $jl$ ) is along  $+\alpha$  direction, the negative means its displacement induces force on atom ( $jl$ ) along  $+\beta$  direction, and vice versa.

In main text Table I, the negative force constant  $k_{xx}$  for the bond  $d_1$  means that when Sn moves into this bond direction (blue arrow along  $+x$  in Fig. S3a), the induced force on Se (red arrow) is oriented along  $+x$ . This is physically reasonable, since the Sn displacement shortens the  $d_1$ , which will repel the Se1 atom. For  $d_2$  bonds, a similar schematic explains the signs just as

simply. Fig. S3b shows a Sn displacement along  $c(+z)$  direction and the forces on surrounding Se atoms. The negative force constant  $k_{zz}$  for  $d_2$  means that the induced forces on Se2 is along the same direction ( $+z$ ) as the Sn displacement. This displacement also induces forces on neighboring Se atoms along the  $b$  direction ( $k_{zy}$ ), which tends to rotate the bonds. This simple picture actually agrees well with the structure evolution from Cmc to Pnma:  $d_2$  bonds become short and the bond angle become larger, while  $d_3$  bonds become longer ( $d_3$  bonds in Pnma phase) and the bond angle become smaller.

---

\* Electronic address: hongj@ornl.gov

† Electronic address: olivier.delaire@duke.edu

- [1] Martin T. Dove, Introduction to Lattice Dynamics, Cambridge University Press, 1993.
- [2] Peter Bruesch, Phonons: Theory and Experiments I: Lattice Dynamics and Models of Interatomic Forces, Springer Berlin Heidelberg, 2012.
- [3] A. A. Mostofi, J. R. Yates, Y.-S. Lee, I. Souza, D. Vanderbilt and N. Marzari Comput. Phys. Commun. 178, 685 (2008)

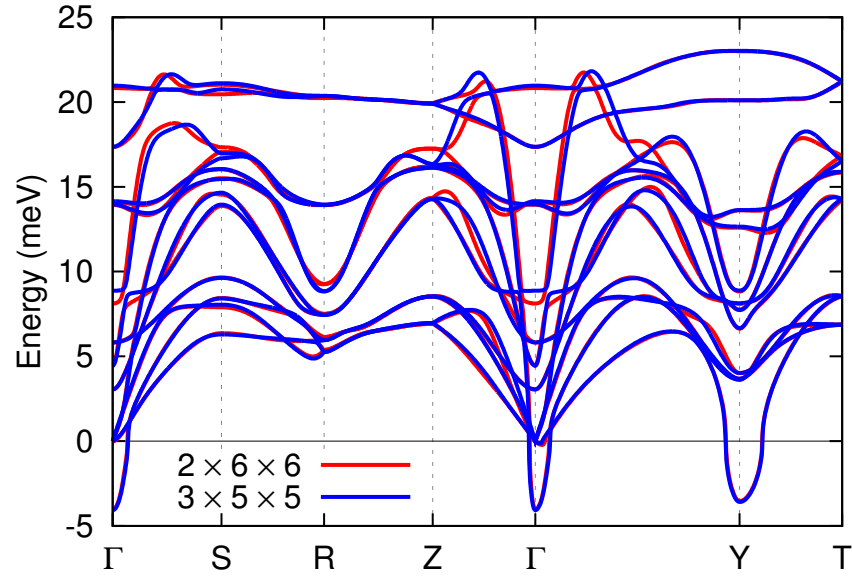


FIG. S1: (Color online) Convergence test for supercell size in-plane. The almost overlapped phonon dispersion curves between two supercell sizes in-plane ( $5 \times 5$  vs.  $6 \times 6$ ) suggest the in-plane size chosen in our calculation is large enough.

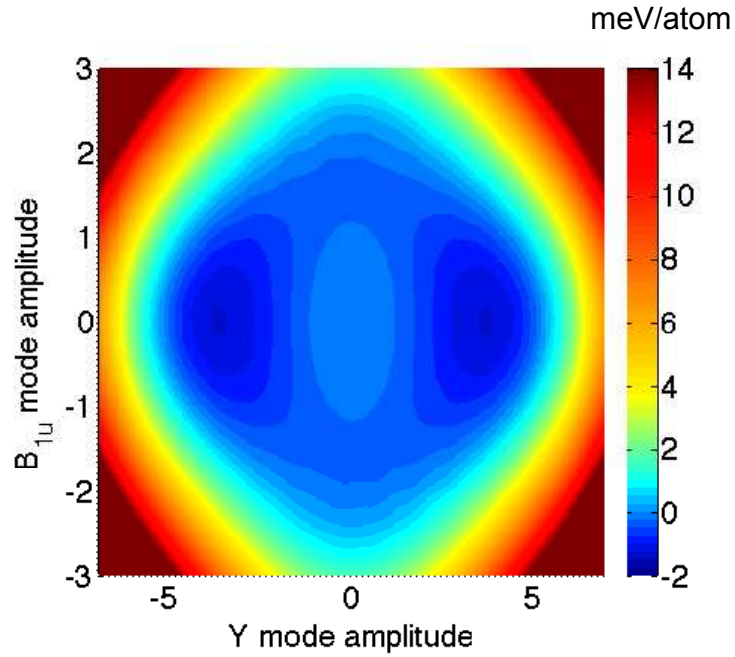


FIG. S2: (Color online) Frozen phonon energy for different coupling between Y and  $B_{1u}$  mode.



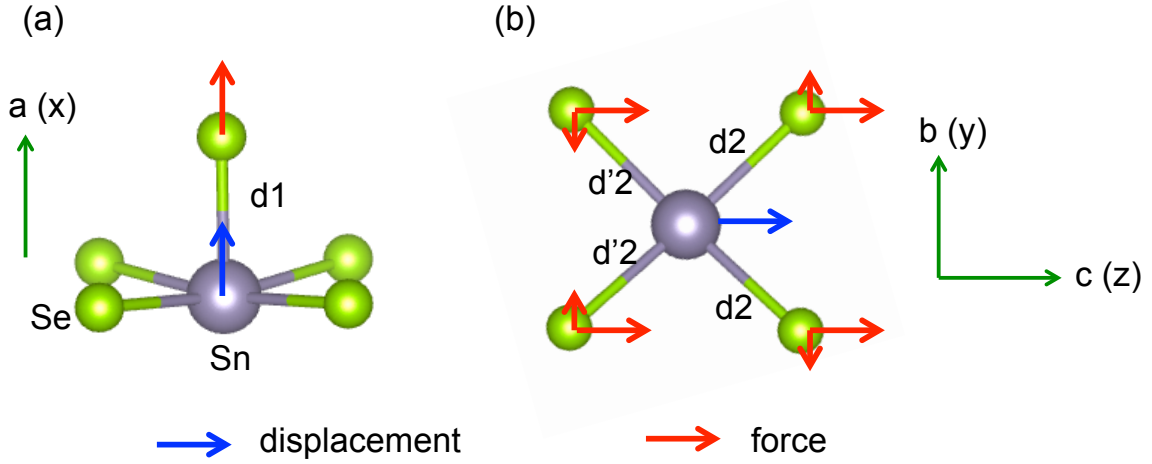


FIG. S3: (Color online) Schematic illustration of negative force constant  $k_{xx}$  for  $d_1$  bond (a) and  $k_{zz}$  for  $d_2$  bonds (b) with Sn displacement (blue arrow). The negative force constant (listed in Table I in main text) indicates the force on Se atoms (red arrow) has the same direction as Sn displacement. Sn displacement along  $+c$  also induces force on surrounding Se atoms along  $b$  direction  $k_{zy}$ , which tends to rotate the bonds, as (b) shows. This simple picture actually agrees well with the structure evolution from Cmc $m$  to Pn $ma$ :  $d_2$  bonds become short and the bond angle become larger, while  $d'_2$  bonds become longer ( $d_3$  bonds in Pn $ma$  phase) and the bond angle become smaller.

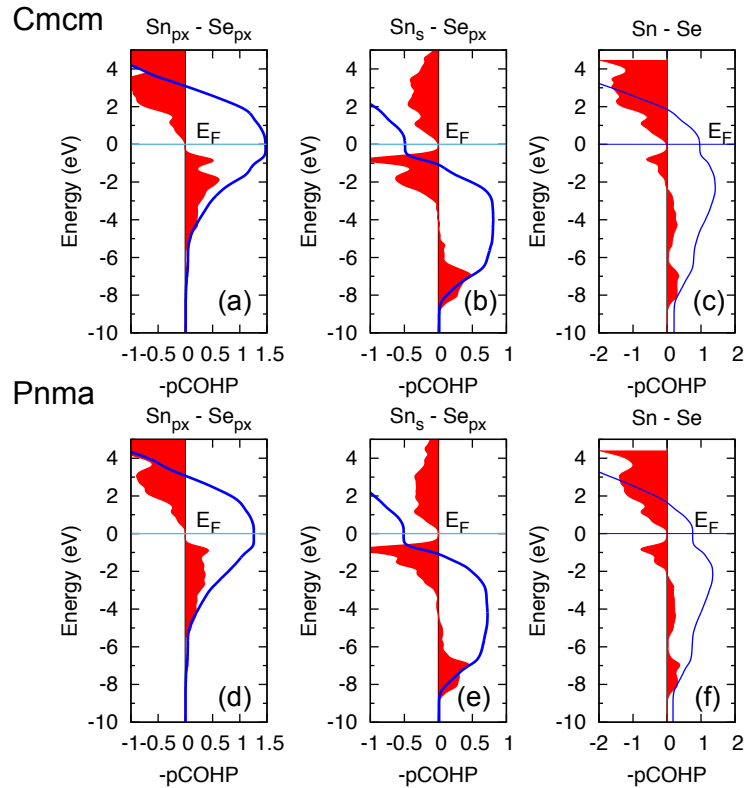


FIG. S4: (Color online) COHP between  $d_1$ . Top panel: axial Sn-Se  $d_1$  bonding in Cmc $m$  phase; bottom panel: axial Sn-Se  $d_1$  bonding in Pn $ma$  phase; (a,d) bonding interaction between axial orbitals Sn- $5p_x$  and Se- $4p_x$ ; (b,e) the bonding and anti-bonding interaction between lone pairs Sn- $5s$  and Se- $4p_x$  orbitals; (c,f) the total bonding interaction between Sn and Se atoms. Red filled curves are the  $-p\text{COHP}$  and the blue curves are the  $-I_p\text{COHP}$ .

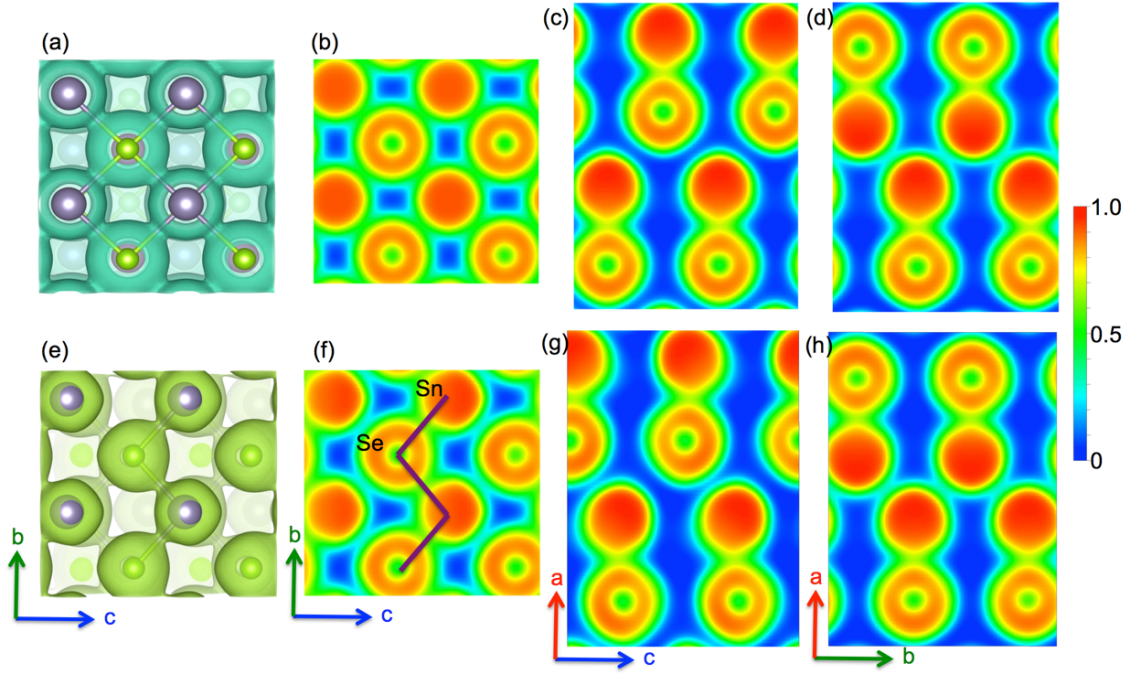


FIG. S5: (Color online) Electron localization functions (ELF) for Cmcm (top panels) and Pnma (bottom panels) phases. (a,e) ELF isosurface in  $b - c$  plane, ELF=0.4 for (a) and ELF=0.6 for (e), Sn atoms are in grey and Se atoms in green; (b,f) is ELF in  $b - c$  plane, (e,g) in  $a - c$  plane and (d,h) in  $a - b$  plane. (c,d,g,h) shows the asymmetric large ELF around Sn along  $a$ , indicating stereochemically active electron lone pairs. (a, b) show ELF is symmetric around Sn in  $b - c$  plane but it becomes active in Pnma phase in (e,f). The positions of Sn and Se atoms and  $d_2$  bonds (brown thick lines) are shown in (f). The red end of the color scale corresponds to high electron localization and the blue end indicates zero zero localization.

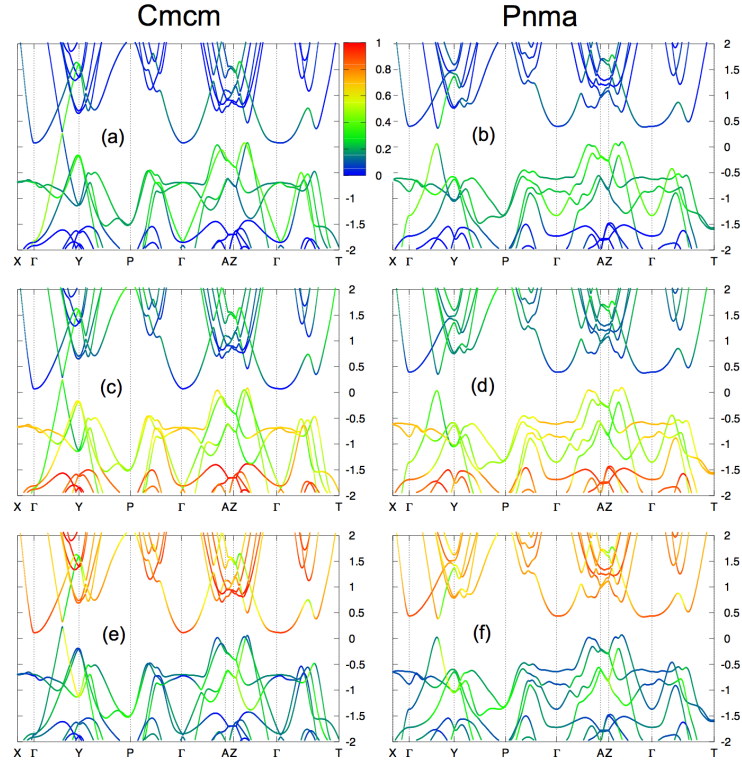


FIG. S6: (Color online) Wannier-interpolated electronic band structure for Cmcm phase (left column) and Pnma phase (right column). Fermi energy is shifted to zero. (a,b) Sn-s orbital weighted; (c,d) Se-4p weighted; (e,f) Sn-5p weighted. Color coding indicates the weight of each orbitals. Wannier-interpolated electronic band structure was calculated by using Wannier90 package. [3]

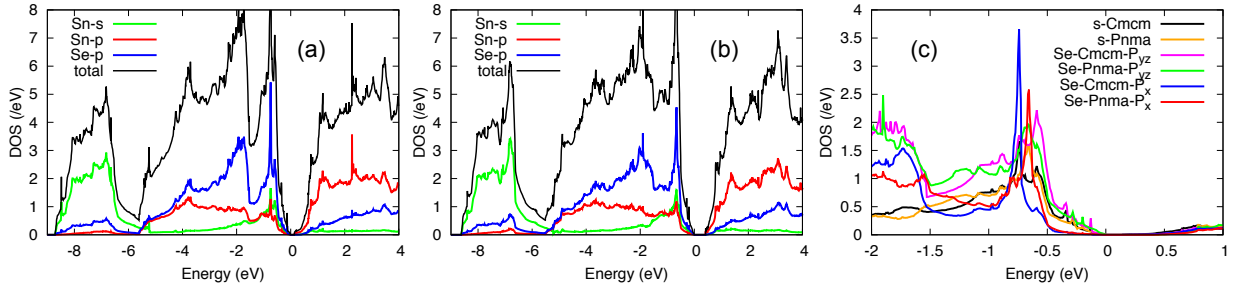


FIG. S7: (Color online) Electronic density of state (DOS) for Cmcm (a) and Pnma (b) phases. (c) is the projected DOS for critical orbitals in both Cmcm and Pnma near Fermi energy which is shifted to zero. Projected Sn *s* and Se *p<sub>yz</sub>* orbitals shift towards lower energy side for Pnma phase, but Se *p<sub>x</sub>* shifts towards high energy level, agrees with COHP analysis.